Cement and Concrete Research 181 (2024) 107545

Contents lists available at ScienceDirect

Cement and Concrete Research

journal homepage: www.elsevier.com/locate/cemconres

An investigation into corrosion around voids at the steel-concrete interface

Miha Hren *, Tadeja Kosec, Andraž Legat

Slovenian National Building and Civil Engineering Institute, Dimičeva ulica 12, 1000 Ljubljana, Slovenia

ARTICLE INFO

Keywords:
Concrete
Mortar
Steel-concrete interface
Coupled multi-electrode array
Electrical resistance sensors
Chlorides
Carbonation
Computed tomography
microCT

ABSTRACT

In this study, the influence of voids on corrosion process at the steel-concrete interface was investigated, as the exact influence of these features on corrosion processes under various environmental conditions is not entirely understood. Coupled multi electrode arrays and electrical resistance probes were implemented to monitor the evolution of corrosion under cyclic exposure to chlorides and carbonation. MicroCT was used to determine the location and volume of corrosion damage. It was found that, in most cases, corrosion damage initiated outside the voids. During initiation and the early propagation phase, the steel beneath the voids rarely participated in the redox reaction. In following phases, various kinds of corrosion evolution were observed. Specific corrosion mechanisms were proposed and discussed to explain these corrosion processes.

1. Introduction

Researchers have identified two processes that most commonly explain how steel in concrete transitions from its passive to its active state [1,2]. The first is the ingress of chloride ions, which may either come from deicing salts, contact with seawater or, in marine environments, from the atmosphere. The critical chloride threshold has been identified as the most important parameter influencing the state of passivation in chloride-contaminated concrete [3]. This is a general parameter, most commonly calculated as the chloride-to-hydroxide ion ratio ($[Cl^-]/[OH^-]$), which describes the state of the mortar around the reinforcement bars. It should be emphasized, however, that significant scatter was observed in the values obtained [3]. The second process, carbonation, also has a heavy impact on the initiation of corrosion. During the hydration of cement, calcium, potassium and sodium hydroxides form and subsequently dissolve. This creates a highly alkaline environment inside the concrete pores, causing a pH value of more than 13. In this type of environment, carbon steel tends to be passive [4]. Over time, however, CO_2 reacts with the pore solution in a process called carbonation. A side effect of carbonation is a reduction in alkalinity, with the pH value dropping to about 9, at which point the steel depassivates and active corrosion may start [4].

The steel-concrete interface (SCI), which represents the layer where steel and concrete are in contact with one another, was identified as a potential parameter influencing corrosion behaviour as early as 1975 [5]. Despite this, however, research investigating its effect on corrosion has not been extensive enough. Angst et al. recently published a literature review on this topic [6], in which they identified the gaps in existing knowledge and discussed the features present at the steel-concrete interface. Fig. 1 shows the different types of voids found at the steel-concrete interface, including air voids, cracks, slips and crevices, as well as the presence of partly-dissolved corrosion products with mill scale. Most of these spatial inhomogeneities are randomly distributed along the steel surface and can cause corrosion processes to behave in a different way compared to how they do in the bulk material.

The two most common types of void around steel rebars are air bubbles and cracks, which are often the result of cement hydration and mechanical stresses, respectively. Both types of voids can either be dry or contain varying levels of liquid and oxygen. In a recently-published review [7], the authors proposed different corrosion mechanisms within voids based on their saturation state. It was suggested that corrosion only initiates inside a void if it is sufficiently saturated with a liquid solution, which, for larger, macroscopic pores in concrete, usually takes years to occur. Additionally, the authors [7] proposed that entrapped oxygen also plays a role, promoting corrosion either inside the void itself or somewhere in its vicinity. Either way, the absence of full contact between the steel and the concrete creates a specific corrosive environment, especially at the transition between the void and the concrete. This area is particularly difficult to study, due to the random location upon which it can manifest, and the lack of accurate,

Abbreviations: SCI, steel-concrete interface; CMEA, Coupled multi-electrode array; ER, Electrical resistance.

* Corresponding author.
E-mail addresses: miha.hren@zag.si (M. Hren), tadeja.kosec@zag.si (T. Kosec), andraz.legat@zag.si (A. Legat).

https://doi.org/10.1016/j.cemconres.2024.107545
Received 15 January 2024; Received in revised form 29 April 2024; Accepted 9 May 2024
Available online 14 May 2024

non-destructive techniques available to characterize it.

Another corrosion phenomenon that can potentially occur at the steel-concrete interface is crevice corrosion. Crevice corrosion is a type of localised corrosion that forms within narrow clearances, beneath corrosion products or shielded metal surfaces [8,9]. These narrow gaps make it difficult to maintain the steady-state oxygen concentration required for a cathodic reaction, resulting in the formation of an anodic site. The characteristics and boundary conditions of crevice corrosion occurring on steel rebars embedded in concrete are not quite clear, since only a few studies on this topic have been completed [10–14]. In nuclear power plants, steel liners embedded in concrete are often used to provide containment, creating a barrier against nuclear radiation. These liners usually come in the form of domes and cylinders and are characterised by a large surface area and poor steel-to-concrete adhesion, making their unique structure potentially vulnerable to crevice corrosion. Very limited information is available about containment liner corrosion, either generally or, more specifically, with respect to crevice corrosion [15–17]. As these containments need to maintain their integrity throughout their lifespan [18,19], information concerning the localised corrosion mechanisms at the steel-concrete interface would be very beneficial.

One of the main reasons for the gap in knowledge in this field of research is a lack of suitable techniques that can be used to monitor and observe corrosion processes on the surface of steel embedded in concrete. As the steel is fully embedded in the concrete, it is impossible to use non-destructive techniques that require access to the steel surface for assessment. Most conventional electrochemical methods also provide very limited or no spatial information regarding the mechanism of corrosion. Nevertheless, a few techniques have emerged over the past two decades that enable the monitoring of steel corrosion in concrete over both space and time. These are detailed below:

I. Coupled Multi-Electrode Arrays (CMEAs) are the most advanced technique used for spatio-temporal measurements of corrosion and are probably best suited for monitoring corrosion mechanisms at the mortar-void interface. This technique is capable of measuring very small corrosion currents on each individual electrode in an array. These electrodes are electronically coupled through Zero Resistance Ammeters (ZRA), making them act as a single uniform surface. As anodic and cathodic areas form on certain electrodes, such activity is accurately detected. In the past, this technique has been successfully used to monitor the corrosion of carbon steel in concrete [20,21], stainless steel in concrete [22] and copper in bentonite [23]. The technique has also been successfully used to monitor crevice corrosion [24–26], but never to study crevice corrosion in concrete.
II. Measurement using electrical resistance (ER) sensors is a physical monitoring technique generally used to monitor the corrosion of steel in concrete over time [27]. As the cross section of the steel electrodes is reduced, information about corrosion is provided based on the changes in the resistance of the ER probe. By positioning several sensors across different locations, information regarding spatial corrosion can also be provided.
III. X-ray microtomography (microCT) is a microscopic technique that uses X-ray images to reconstruct the cross sections of an object. It can be used to non-destructively examine and monitor steel corrosion, the microstructure of concrete and, to a lesser extent, the steel-concrete interface [20,28]. It not only provides the location and shape of any corrosion damage, but can also be used to quantify corrosion damage using volume segmentation techniques.

The primary goal of this study was to characterize the initiation and early propagation phase of corrosion processes around the mortar-void-steel interface. A combination of CMEA, ER and microCT techniques was utilized for this purpose, measuring the corrosion of steel in specially prepared OPC mortar specimens in which artificial voids had been created. These specimens were exposed to cyclic wetting and drying and monitored for up to 52 weeks. Corrosion was initiated by wetting the mortar with chloride solution and through the use of carbonation, thus creating 4 specific exposure environments: non-carbonated without chlorides, non-carbonated with chlorides, carbonated without chlorides and carbonated with chlorides. Special emphasis was placed on the position of the anodic and cathodic locations relative to the location of the void, the size of the corrosion current densities inside and outside the void, and the distribution of the corrosion damage surrounding the void. The results from CMEA and ER analysis were further verified by X-ray computed microtomography, with the corrosion damage determined from measuring the anodic currents being compared to that obtained from microCT analysis. An attempt was made to explain the specific corrosion mechanisms around the void.

2. Materials and methods

2.1. Specimen preparation

To evaluate the corrosion processes at the mortar-void interface, two types of mortar specimens were produced, each designed to accommodate their respective techniques. The first set were CMEA specimens, which consisted of 25 carbon steel electrodes, 0.5 mm in diameter, arranged in a 5 × 5 array. The electrodes were embedded in epoxy resin and placed in a 3D-printed housing (Fig. 2a). These specimens needed to be suitable for corrosion measurements by CMEA, while still remaining sufficiently small and compact to also be examined by microCT. The exposed area of the wire cross-section was ground with sandpaper (up to 2500-grit) and the electrodes degreased using acetone. A pool was made on top of the electrodes for casting the mortar, including a hole for a PTFE strip (Fig. 2b). A total of 8 CMEA specimens were produced across four groups, with 2 specimens in each group exposed to identical conditions in terms of chloride and carbonation. Due to the complexity of the CMEA analysis, only 1 of the 2 identical specimens was chosen for a detailed temporal analysis for each exposure condition, while all 8 specimens were analysed in spatial (array) form and included in the discussion. The four CMEA specimens that were analysed in greater detail are CMEA-2, CMEA-3, CMEA-6 and CMEA-8. For the rest of the specimens, the temporal graphs are available as supplementary material.

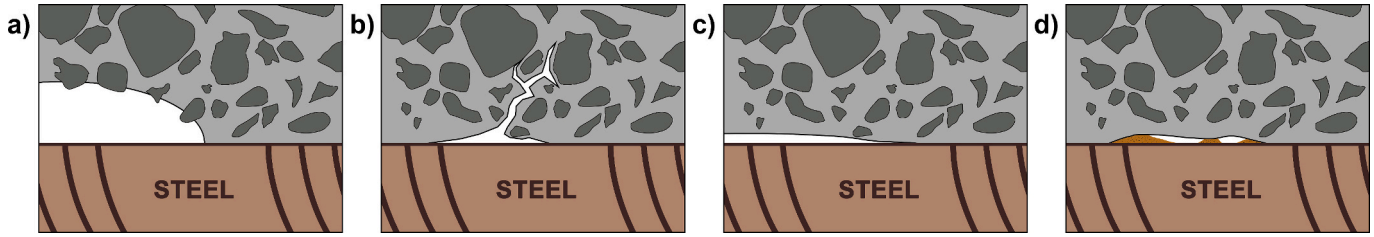

Fig. 1. Different features at the steel-concrete interface: a) air voids, b) cracks, c) slips and crevices, and d) corrosion products and mill scale in a void.

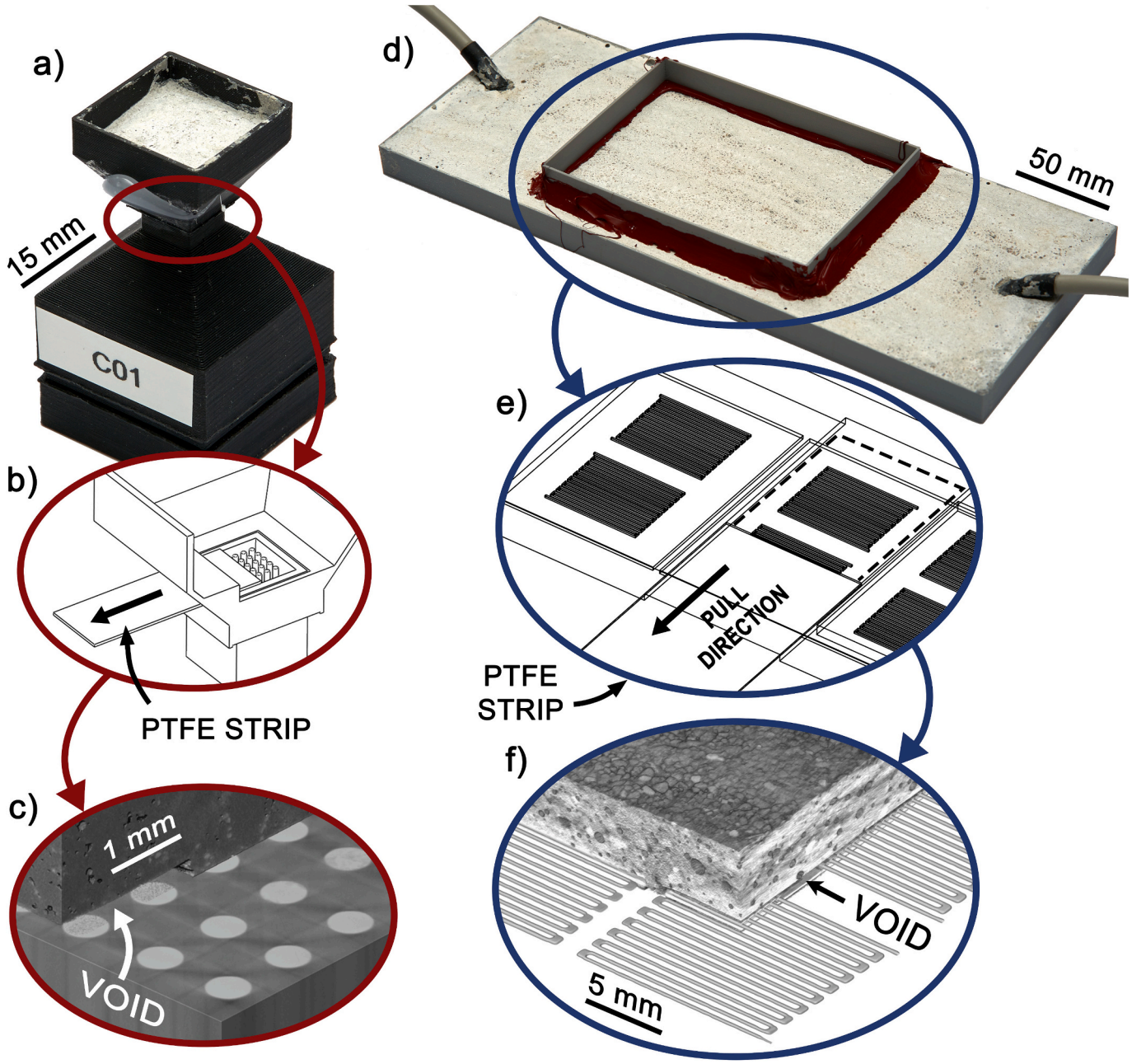

Fig. 2. Examples of the CMEA (a) and ER (d) specimens, with a schematic representation of how the void was formed using a PTFE strip (b and e). MicroCT scans showing two examples of voids formed on the CMEA (c) and ER (f) specimens.

The second group of specimens was designed for the ER corrosion monitoring experiments (Fig. 2d). 3D printed moulds were made for the ER sensors, with two carbon steel sensors fastened to the floor of the moulds in each specimen. The exposed sections of the two sensors were placed close to one another without coming into direct contact, thus simulating a continuous steel surface (Fig. 2e). A hole was made in the mould on either side of one sensor to accommodate a PTFE strip. A total of 12 ER specimens were produced, designated ER-01 to ER-12. An overview of all the specimens and their major properties can be found in Table 1.

The mortar used in this research, designated as CEM I, was prepared using ordinary Portland cement (OPC) in accordance with the standard EN 197–1:2011 [29]. The mortar was prepared using a water-to-binder ratio of 0.6 and a cement-to-aggregate ratio of 1:4. Additionally, the aggregate used was in accordance with the standard for determining the strength of cements [30]. The concrete cover was 10 mm in all specimens. The quality and microstructure of the steel sheet and steel wires used in this research are described in detail in our previous work [31].

Before the mortar was cast into the prepared specimens, PTFE strips were placed to cover parts of the exposed sensors, in order to create a void between the mortar and the steel surface. In the case of the CMEA specimens, the PTFE strips covered 40 % of the electrodes (i.e. a 2 × 5 array), leaving 60 % (a 3 × 5 array) in good contact with mortar (Fig. 2b). In the case of the ER specimens, the PTFE strip completely covered one of the two ER sensors, leaving the other in good contact with the mortar (Fig. 2e). Once the mortar was sufficiently solid (approx. 12 h after casting), the PTFE strips were pulled away from beneath the mortar, leaving behind voids between the mortar and the surface of the electrode. The width of the void, measured using the microCT technique, was 0.3 mm for the CMEA specimens and 0.5 mm for the ER specimens. The holes left by the strips on the specimen surface were then

Table 1
List of specimens, indicating the technique used, the conditions of exposure (accelerated carbonation and/or wetting with chlorides), the time of exposure and steel type.

Specimens	Technique	Carbonated	Chlorides	Exposure time	Working electrode
CMEA-1, CMEA-2	CMEA	No	No	25 weeks	5 × 5 wire
CMEA-3, CMEA-4	CMEA	No	Yes	25 weeks	5 × 5 wire
CMEA-5, CMEA-6	CMEA	Yes	No	25 weeks	5 × 5 wire
CMEA-7	CMEA	Yes	Yes	16 weeks	5 × 5 wire
CMEA-8	CMEA	Yes	Yes	25 weeks	5 × 5 wire
ER-01, ER-02, ER-03	ER	No	No	52 weeks	etched sheet
ER-04, ER-05, ER-06	ER	No	Yes	52 weeks	etched sheet
ER-07, ER-08, ER-09	ER	Yes	No	52 weeks	etched sheet
ER-10, ER-11, ER-12	ER	Yes	Yes	52 weeks	etched sheet

covered using silicone so as to prevent oxygen and humidity in the air from directly entering the voids.

The shape, size and location of the voids in both the CMEA specimens (Fig. 2c) and ER specimens (Fig. 2f) were verified using microCT scans. It is important to note that, as expected, the microCT scans did not show any visible gaps between the good mortar contact and the sensor surface. This verification is, however, limited by the resolution of the microCT, meaning there is a possibility that gaps smaller than 10 μm (in the CMEA specimens) or 50 μm (in the ER specimens) were also present in the specimens designated as having good contact with the mortar.

2.2. Curing and carbonation

Following the processes of casting and void formation, the mortars were cured at a temperature of 20 ± 2 °C and a relative humidity of 100 % for 28 days before any further corrosion-initiating exposure was introduced. In addition, half of the specimens were subjected to accelerated carbonation conducted in an environmental chamber, where they were exposed to a CO_2 concentration of 3.1 % at a relative humidity of 57 % and a temperature of 25 °C. The level of carbonation was monitored using supplementary mortar cylinders of 60 mm in diameter. The specimens were periodically cracked and tested using the phenolphthalein test in order to ensure that a carbonation depth of at least 10 mm was achieved. The accelerated carbonation period ended after 14 weeks of exposure. During the accelerated carbonation process, the non-carbonated specimens were kept in a laboratory at an air temperature of 22 ± 2 °C and a relative humidity of 50 ± 5 %. Throughout the rest of this article, these specimens will be referred to as carbonated and non-carbonated, respectively.

2.3. Chloride contamination and corrosion monitoring

To initiate corrosion, either tap water or a 3.5 % NaCl solution were introduced through cyclic ponding throughout the corrosion monitoring period. Table 1 shows which specimens were exposed to wetting with chlorides. A 3D printed wetting pool was placed on the upper side of each specimen (Fig. 2a and b), with weekly cycles consisting of 2 days wetting followed by 5 days drying. At the start of each drying period, any remaining solution in the pool was absorbed using a pipette in order to accelerate the drying process. As stated previously, corrosion was then monitored using both the Coupled Multi-Electrode Array (CMEA) technique and Electrical Resistance (ER) sensors.

2.3.1. Coupled multi-electrode array (CMEA)

Corrosion was continuously monitored using custom-made Zero Resistance Ammeters (ZRAs). All specimens were measured for 25 weeks, except for specimen CMEA-7, which was measured for 16 weeks due to early termination of the experiment (see Table 1). The ZRAs consisted of 25 individual ammeters coupled together via steel electrodes, comprising a 5 × 5 array at one end and a common floating ground on the other. Together, these components formed the CMEA monitoring system. Fig. 3a shows a schematic representation of the CMEA system, including the artificially-formed cross-sectional void. The artificial void was formed over a 2 × 5 array of electrodes, with the other 3 × 5 array remaining in good contact with the mortar. As anodic and cathodic sites are formed on the various coupled steel electrodes, they become subjected to the flow of positive or negative corrosion currents, as do the individual ZRAs. Each current recorded thus represents either an anodic or cathodic current flowing through a certain electrode. In the ZRA system utilized, positive currents represent anodic currents while negative currents represent cathodic currents. More details regarding how other authors have implemented similar ZRA systems for CMEA or electrochemical noise measurements can be found in [32,33].

The measurement frequency for each mortar specimen was set at 1 Hz. The detectable current ranged from a minimum of −5 μA to a maximum of +5 μA, with a precision of 150 pA per electrode. Considering the electrode diameter (0.5 mm), this corresponded approximately to a maximum measurable current density of ±2.5 mA/cm^2, with a resolution of 76 nA/cm^2. Eq. (1) [34] was used to calculate the corrosion rate (v_{corr}, in μm/year) from the corrosion current density (j_{corr}, in μA/cm^2). The following values were used as constants: molar mass M = 55.845 g/mol, oxidation number $z = 2$, density ρ = 7.85 g/cm^3 and a constant of 3.27 in μm g/μA cm year, as obtained from Faradays Law.

$$v_{corr} = \frac{3.27M}{z\,\rho} j_{corr} \quad (1)$$

Another assumption in the corrosion rate calculations was made, presuming that the corrosion damage was uniformly distributed across the entire cross-section of each electrode. To achieve results more akin to those obtained through microCT, the corrosion damage at the conclusion of the exposure was also calculated according to the reduction in volume of each electrode, by integrating the corrosion current over time and calculating corrosion damage using Eq. (1). It should be noted that the CMEA technique cannot detect self-corrosion, a process where the anodic and cathodic currents are located on the same electrode. CMEA and microCT techniques will thus show slightly different results.

2.3.2. Electrical resistance (ER) sensors

Throughout the 52-week period of exposure corrosion was monitored by ER sensors. Measurements were made once per week, at the end of the wetting cycle. The ER sensors consisted of an etched steel plate, with two Wheatstone bridge resistors representing the exposed steel surface. Fig. 3c presents a schematic of the Wheatstone bridge, with the position of the resistors labelled, while Fig. 3b shows the ER sensor with both the protected (R) and exposed (R_x) resistors visible. The resistors are made of a long, thin, steel conductor, with the cross-section reducing as the steel corrodes. The protected resistors are made of the same material as the exposed working electrodes and are used to compensate for fluctuations in temperature and electrical current. A more detailed description, including operation of the ER sensor, can be found in [27,35,36].

Weekly measurements of ER sensors were conducted by employing a custom-made current generator to apply a 50 mA current to the probe. Two voltage readings were acquired using a Fluke 289 multimeter: the U_{12} voltage, measured across points 1 and 2, and the U_{34} voltage, measured across points 3 and 4 (refer to Fig. 3c). Subsequently, the methodology outlined in [35] was applied to compute the reduction in thickness and corrosion rate.

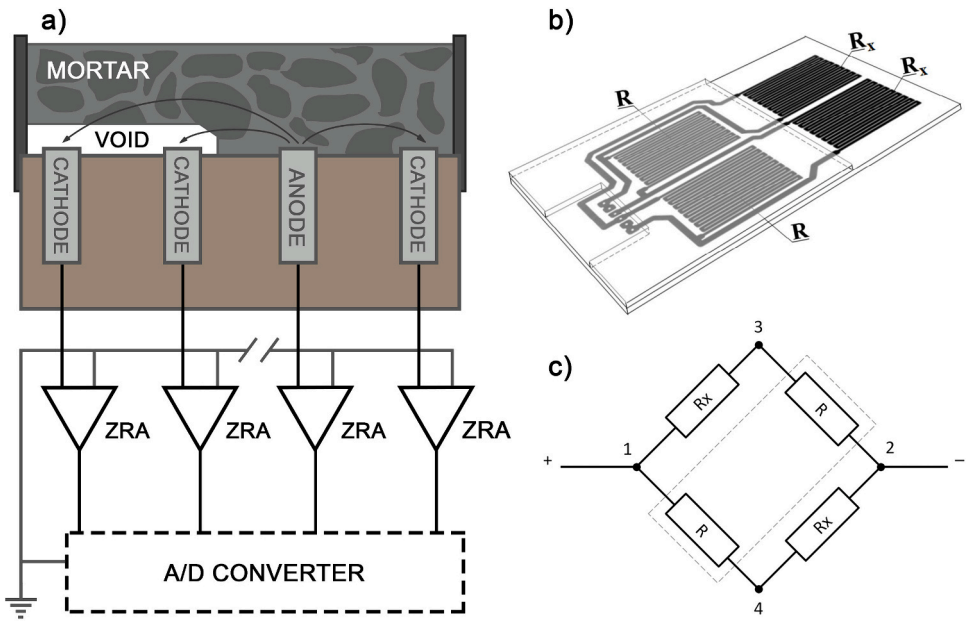

Fig. 3. (a) schematic representation of the Coupled Multi-Electrode Array (CMEA) system, (b) the Electrical Resistance (ER) sensor, and (c) the principle of operation of the Wheatstone bridge used in the ER sensors.

2.4. Post-exposure validation

At the end of the corrosion monitoring period, both the CMEA and ER specimens were non-destructively examined using an Xradia microXCT-400 microCT scanner (Xradia, 2012, USA). Sections of the specimens were scanned at 150 kV and 10 W, using a macro-objective with 0.71× magnification. A High Energy #1 filter was used for the CMEA specimens and a Low Energy #3 filter for the ER specimens. The voxel sizes obtained were 8 μm for the former and 55 μm for the latter. 3D images were analysed and visualised using Dragonfly software (Comet Technologies, 2023, Canada).

3. Results

3.1. Coupled multi-electrode arrays

3.1.1. Spatial distribution of the anodic and cathodic currents

The corrosion currents on 8 mortar specimens, made from the CEM I mortar in either a non-carbonated or carbonated state, were monitored for 25 weeks using the CMEA technique. Half the specimens were exposed to cyclic wetting with tap water, while the other half were exposed to cyclic wetting using a 3.5 % NaCl solution. This created four specific exposure environments: non-carbonated without chlorides, non-carbonated with chlorides, carbonated without chlorides and carbonated with chlorides.

The average anodic and cathodic corrosion current densities are summarized in Fig. 4. The specimens are grouped in quadrants, with each quadrant representing a specific exposure environment. The results are shown in array form, where the red matrices represent the anodic corrosion currents for each specimen, while the green matrices represent the cathodic corrosion currents for each specimen. The light grey circles indicate that no corrosion activity occurred at the electrode. The dashed blue line represents the group of 2 × 5 electrodes where the artificial void was created. The rows (1 to 5) and columns (A to E) of each array of electrodes are labelled accordingly. The same label nomenclature is used throughout this article to describe the particular electrodes of any given array. Specimens that were chosen for detailed temporal examination have a red square surrounding their label.

Where no chlorides were present (as shown in the upper two quadrants in Fig. 4), the behaviour of the carbonated and non-carbonated mortars was similar. Almost all the anodic activity occurred where there was good contact with the mortar, where corrosion was moderately localised. The average corrosion rates on the most anodic electrodes were between 0.7 and 0.9 μA/cm^2 in all specimens. Cathodic activity also predominantly occurred where there was good contact with the mortar, where the most anodic electrodes also showed the highest amount of cathodic activity. In general, the corrosion activity of electrodes positioned beneath the void was negligible in the specimens not exposed to chlorides.

With the addition of chlorides, corrosion became more localised, with higher anodic corrosion currents on the most anodic electrodes. Specimens in the non-carbonated mortar (Fig. 4, bottom left quadrant) showed higher average anodic currents compared to specimens without chlorides, reaching a value of 2.5 μA/cm^2 on the most active electrode (A1) for CMEA-3 specimen, and 3.7 μA/cm^2 on the most active electrode (A2) for CMEA-4 specimen. As with the non-chloride specimens, both the anodic and cathodic activity primarily occurred where there was good contact with the mortar, whereas electrodes positioned beneath the void participated in the anodic and cathodic corrosion activity only to a minor degree. As noticed previously, the electrodes which exhibited high anodic activity (e.g., A1 electrode in both specimens) tended to also exhibit high cathodic activity in this environment.

In contrast to in the other 3 environments, significant corrosion activity was observed in the carbonated mortar wetted with chlorides (Fig. 4, bottom right quadrant), both where there was good contact with the mortar as well as where there was contact with the void. The anodic current density for the CMEA-7 specimen reached a value of 11.8 μA/cm^2 under the mortar, and a value of 2.6 μA/cm^2 next to the void, while the values for CMEA-8 specimen were 3.3 μA/cm^2 under the mortar and 5.3 μA/cm^2 next to the void. These higher corrosion currents made carbonated environment with chlorides the most corrosive environment tested. The highest cathodic activity was also distributed across the electrodes positioned both under the void and next to the mortar.

3.1.2. Corrosion propagation over time

To show the temporal response of the CMEA experiment, 1 specimen from each of the 4 exposure conditions was chosen for detailed analysis. The results are presented in Figs. 5–8. Up to 8 of the most active / participating electrodes were emphasized with coloured lines in order to obtain a better representation of the corrosion activity on the specimen.

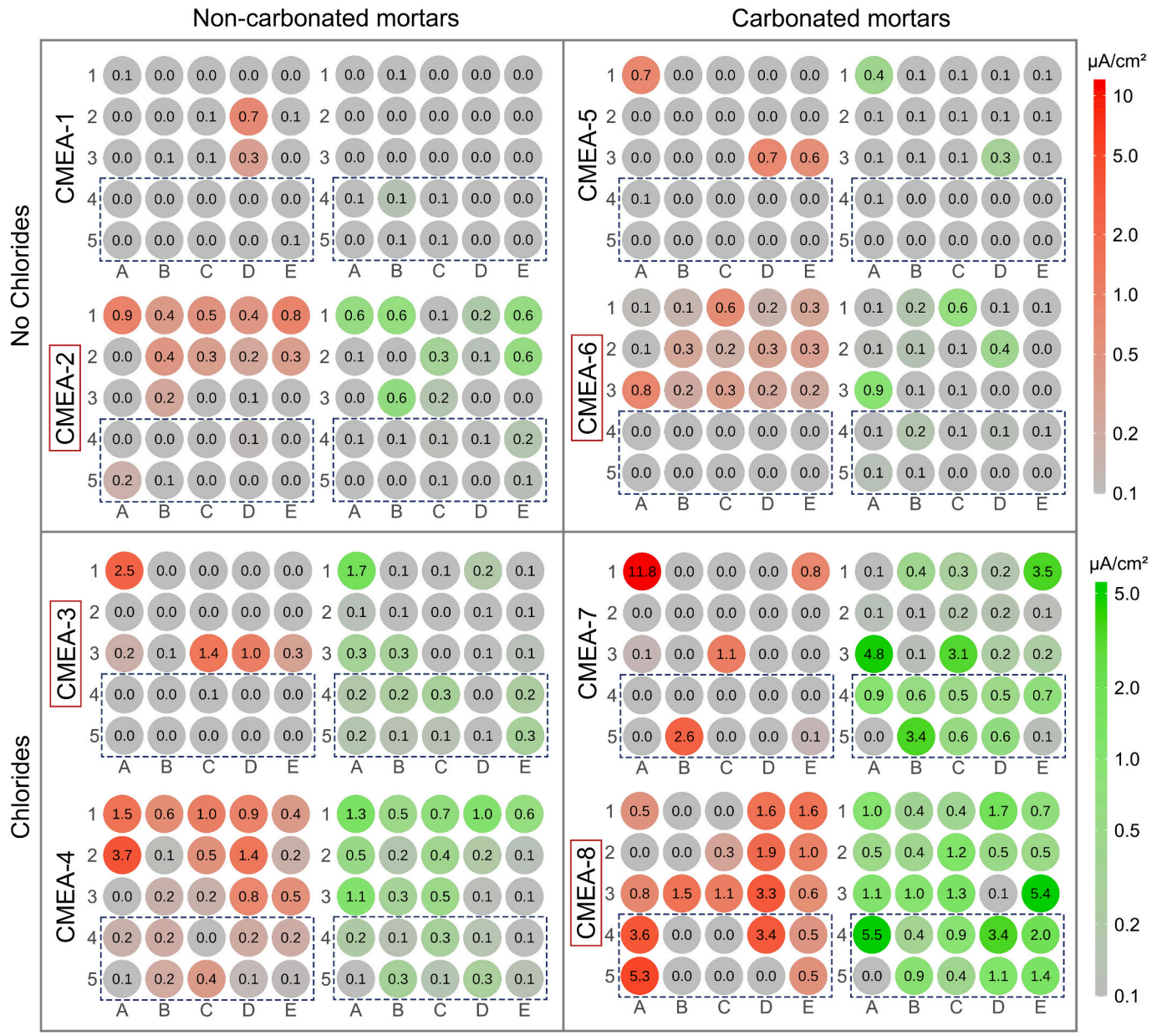

Fig. 4. Average corrosion current densities measured on the 8 specimens throughout the cyclic wetting exposure. Each quadrant represents a specific exposure environment. The red arrays represent anodic currents on any given specimen, while the green arrays represent cathodic currents. The colour scale is logarithmic. The electrodes positioned directly beneath the void are indicated by the rectangle marked with a blue dashed line. Specimens that were chosen for detailed temporal examination have a red square surrounding their label. (For interpretation of the references to colour in this figure legend, the reader is referred to the web version of this article.)

The electrodes in contact with the mortar are represented by solid lines, while the electrodes positioned beneath the void are represented by dashed lines. Each figure is also equipped with a matrix diagram showing the colour represented by each electrode, an array of the average corrosion rates across the entire exposure period, and light blue lines representing the wetting periods, with the consecutive cycle numbers outlined above.

Fig. 5 shows the corrosion current densities for the non-carbonated specimen without exposure to chlorides (CMEA-2). Corrosion initiated after 9 weeks of exposure, during the 10th wetting cycle. Between cycles 10 and 15, several electrodes under good contact with the mortar (e.g. B3, C2 and E2) were anodic over a single wetting cycle, but then became cathodic in one of the consequent cycles. Only after cycle 15 did electrodes A1 and E1 become anodic for multiple successive cycles, whilst several other electrodes also in contact with the mortar remained cathodic. Each wetting cycle showed a repeating pattern (Fig. 5d), whereby the corrosion current of an anodic electrode spiked when wetting was initiated, started dropping as the oxygen became depleted, then spiked again shortly after the start of the 5-day drying period. During the spikes, the corrosion rates briefly reached values of 500 μm/year. Overall, the corrosion behaviour of the CMEA-2 specimen in good contact with the mortar is typical of uniform corrosion with some localised areas, whereas the anodic and cathodic corrosion activity directly under the void remained comparatively low.

Fig. 6 shows the corrosion current densities for the non-carbonated specimen with chlorides (CMEA-3). Corrosion initiation started immediately; beginning in the 1st wetting cycle and continuing up until week 19, electrode A1 was consistently anodic, even during the drying periods. The average corrosion rate on this electrode was around 50 μm/year, with short-term peaks reaching approximately 150 μm/year.

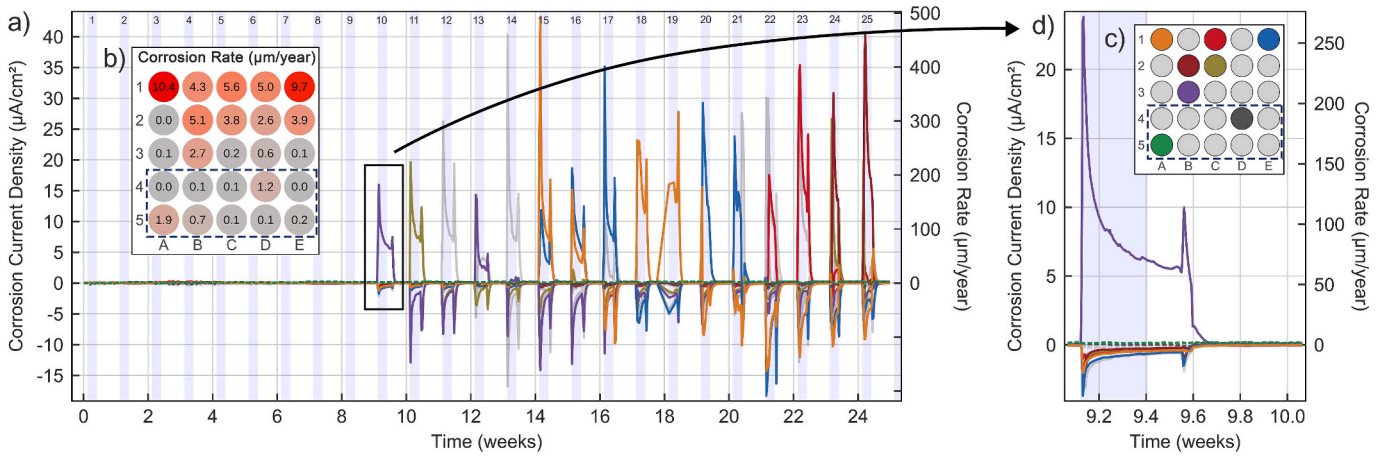

Fig. 5. (a) Corrosion current densities measured on the 25 electrodes of the CMEA-2 specimen (non-carbonated, no chlorides). (b) An array showing the average corrosion rates across the entire period of exposure. (c) The most active electrodes are shown in colour. The electrodes beneath the void are indicated by the rectangle marked with a blue dashed line. (d) Detailed view of a typical wetting cycle, when corrosion initiates, as marked on graph (a) with a black rectangle. (For interpretation of the references to colour in this figure legend, the reader is referred to the web version of this article.)

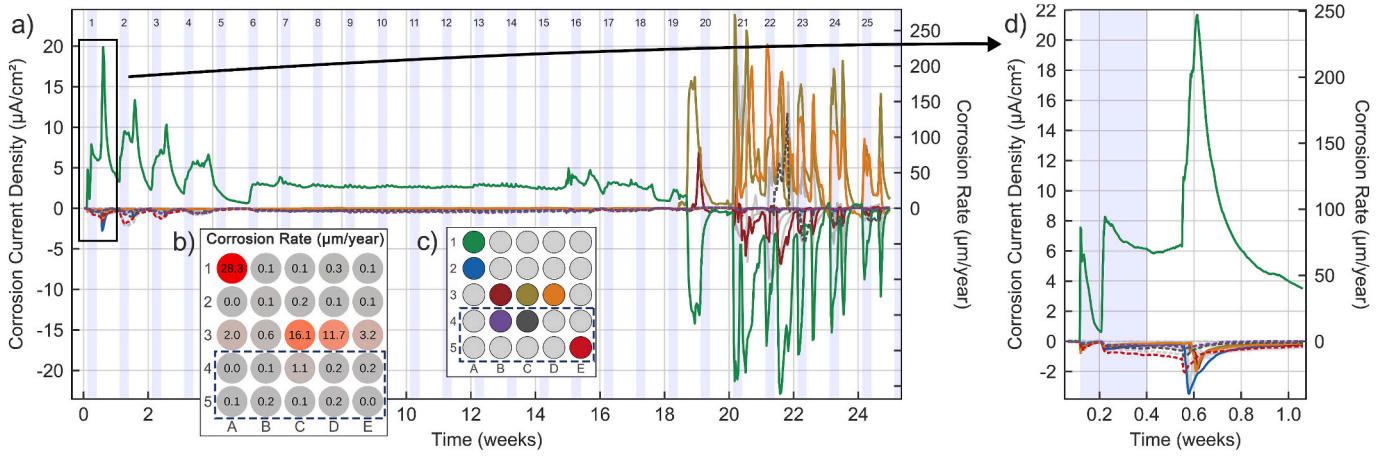

Fig. 6. (a) Corrosion current densities measured on the 25 electrodes of the CMEA-3 specimen (non-carbonated, with chlorides). (b) An array showing the average corrosion rates across the entire period of exposure. (c) The most active electrodes are shown in colour. The electrodes beneath the void are indicated by the rectangle marked with a blue dashed line. (d) Detailed view of a typical wetting cycle, when corrosion initiates, as marked on graph (a) with a black rectangle. (For interpretation of the references to colour in this figure legend, the reader is referred to the web version of this article.)

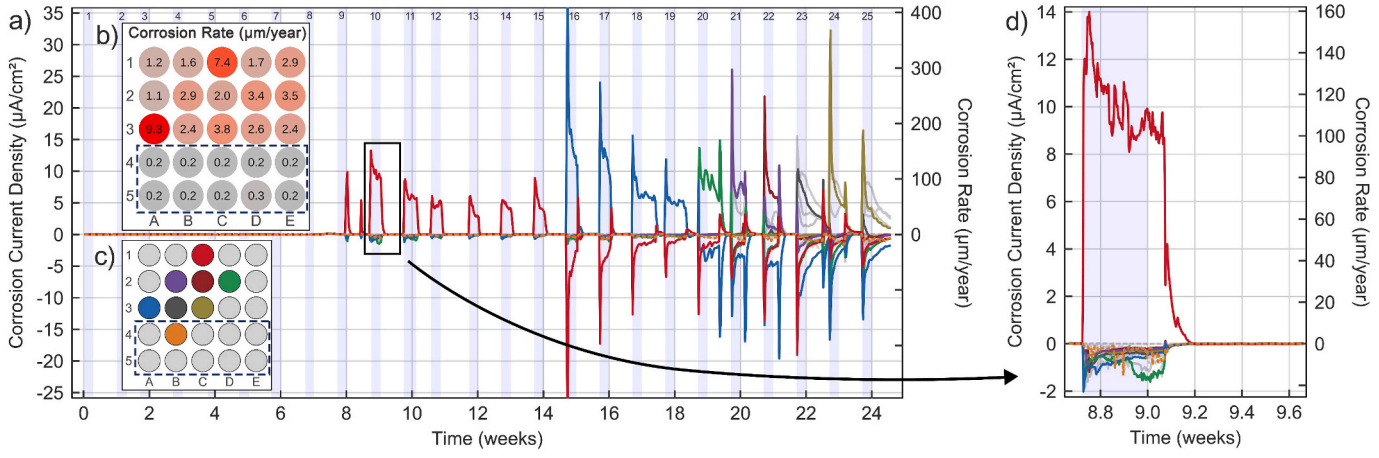

Fig. 7. (a) Corrosion current densities measured on the 25 electrodes of the CMEA-6 specimen (carbonated, no chlorides). (b) An array showing the average corrosion rates across the entire period of exposure. (c) The most active electrodes are shown in colour. The electrodes beneath the void are indicated by the rectangle marked with a blue dashed line. (d) Detailed view of a typical wetting cycle, when corrosion initiates, as marked on graph (a) with a black rectangle. (For interpretation of the references to colour in this figure legend, the reader is referred to the web version of this article.)

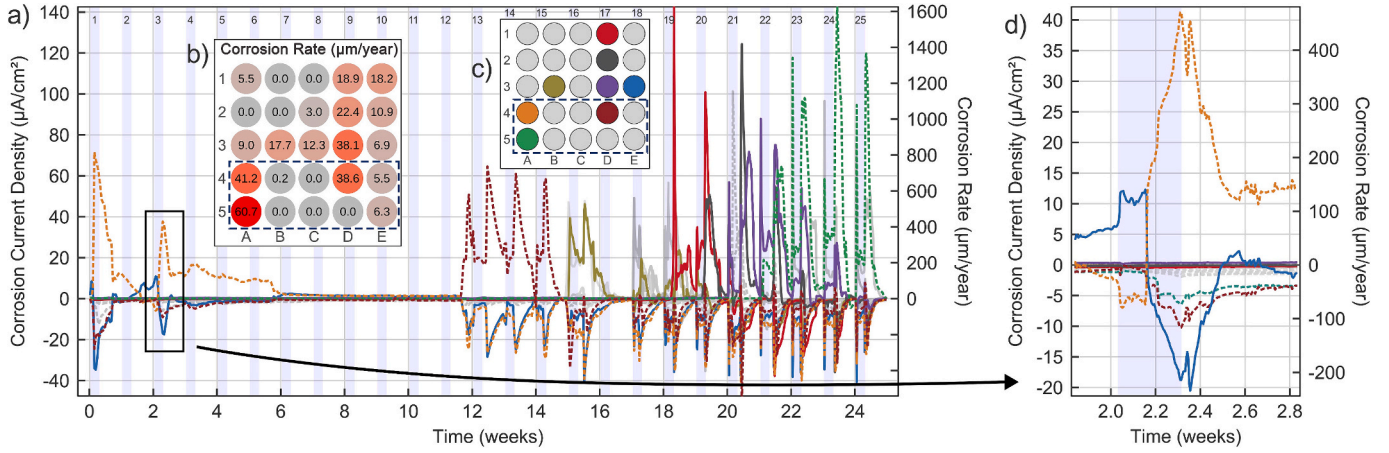

Fig. 8. (a) Corrosion current densities measured on the 25 electrodes of the CMEA-8 specimen (carbonated, with chlorides). (b) An array showing the average corrosion rates across the entire period of exposure. (c) The most active electrodes are shown in colour. The electrodes beneath the void are indicated by the rectangle marked with a blue dashed line. (d) Detailed view of a typical wetting cycle, when corrosion initiates, as marked on graph (a) with a black rectangle. (For interpretation of the references to colour in this figure legend, the reader is referred to the web version of this article.)

During this period, the main cathodic reactions occurred on the void-covered electrodes E5, C4 and B4. The behaviour described is typical of pitting corrosion. After week 19, other electrodes (D3 and C3) also started to exhibit (localised) anodic behaviour, while the A1 electrode started to behave almost exclusively cathodically. Virtually all the anodic and cathodic corrosion activity occurred beneath the mortar during this period, with the exception of the electrode C4, which briefly became anodic after cycle 22.

Fig. 7 shows the corrosion current densities for the carbonated specimen without chlorides (CMEA-6). On electrode C1 (beneath the mortar), corrosion initiated after 8 weeks of exposure. The corrosion was localised, but, unlike consistent pitting corrosion, the anodic reaction only reactivated during the wetting cycles then died down during the drying cycles (Fig. 7d). Wetting cycle 16 pushed the C1 electrode towards the cathodic region, while another electrode (A3) became activated anodically. Similar to electrode C1, the behaviour of the A3 electrode was localised and it transitioned to cathodic behaviour after 4 wetting cycles. Starting from the 20th cycle, several other electrodes beneath the mortar became anodic, which was more akin to uniform corrosion. The cathodic reactions also occurred almost exclusively beneath the mortar throughout the entire exposure period. Of the electrodes positioned directly under the void, only the B4 electrode became slightly cathodic, during the second part of the exposure, while no anodic activity was recorded directly under the void.

Fig. 8 shows the corrosion current densities for the carbonated specimen with chlorides (CMEA-8). As with the non-carbonated specimen with chlorides (Fig. 6), corrosion initiated (on electrode A4) immediately after the first wetting cycle. Corrosion was localised and persisted through multiple wetting and drying cycles, which is indicative of pitting corrosion. Unlike its non-carbonated counterpart, however, the corrosion initiated under the void as opposed to under the mortar. Indeed, the second electrode to exhibit anodic (localised) behaviour (electrode D4), which initiated after wetting cycle 12, was also positioned under the void. From cycle 16 onwards, several other electrodes, positioned both beneath the mortar (B3, D1, D3) and under the void (A5), started to behave anodically and show signs of localised corrosion. Throughout the exposure, cathodic activity was distributed more evenly between the void and mortar areas of the electrodes, slightly favouring the former.

3.1.3. MicroCT post-exposure validation

At the end of the 25-week period of exposure, non-destructive post-exposure analysis was conducted on the 8 CMEA specimens using a microCT scanner, the results of which are presented in Fig. 9. The specimens are grouped in quadrants, with each quadrant representing a specific exposure environment. The image on the left of each specimen shows a cross section of the specimen with the void, mortar and steel electrodes all visible. The location of the cross section is identified on the 3D image (red line), which gives a visual representation of the corrosion damage according to microCT scanning. For select electrodes, damage volumes were obtained using the microCT technique, by calculating the difference between the initial volume of the electrodes and their volume after the corrosion damage had occurred. Due to limits in the microCT resolution, most of the electrodes could not be quantified if their calculated damage from the CMEA technique was below 1×10^6 μm^3, so the comparison will only be done qualitatively, by comparing these 3D images with the average anodic corrosion current densities shown in Fig. 4.

A qualitative comparison of the results shows that, on most of the electrodes, the damage calculated using the CMEA technique is comparable to the visual damage obtained using the microCT technique. There are no indications of crevice corrosion between the protective epoxy and the steel, as most of the electrodes exhibit corrosion damage along their cross section rather than along the length of their side. The discrepancies that exist between the visual representation and the calculated damage can be explained by the low overall amount of damage on most of the electrodes, which increases the margin of error as a result of limits in the microCT resolution.

Heavily damaged electrodes were analysed quantitatively, and the results are presented in Table 2. Results of the CMEA and microCT techniques appear to be well matched, with the values of corrosion damage calculated from the CT scans being approximately 20 to 30 % higher. This error is common, as the CT scan is limited by its resolution, meaning a slight overestimation is made so as to err on the side of caution. Additionally, microCT will also capture any damage that occurs due to self-corrosion in the electrodes (where cathodic and anodic locations exist on the same electrode). Self-corrosion is not recorded by the CMEA technique, so it is always expected that the damage estimated by microCT will be slightly higher than that estimated from the CMEA measurements. A clear example of self-corrosion is electrode A1 on CMEA-7 specimen, as it is common for self-corrosion to occur along the side of the electrode.

3.2. Electrical resistance sensors

3.2.1. Thickness reduction over time

The reduction in thickness of the electrical resistance (ER) sensors was monitored for 52 weeks on 12 mortar specimens made from CEM I

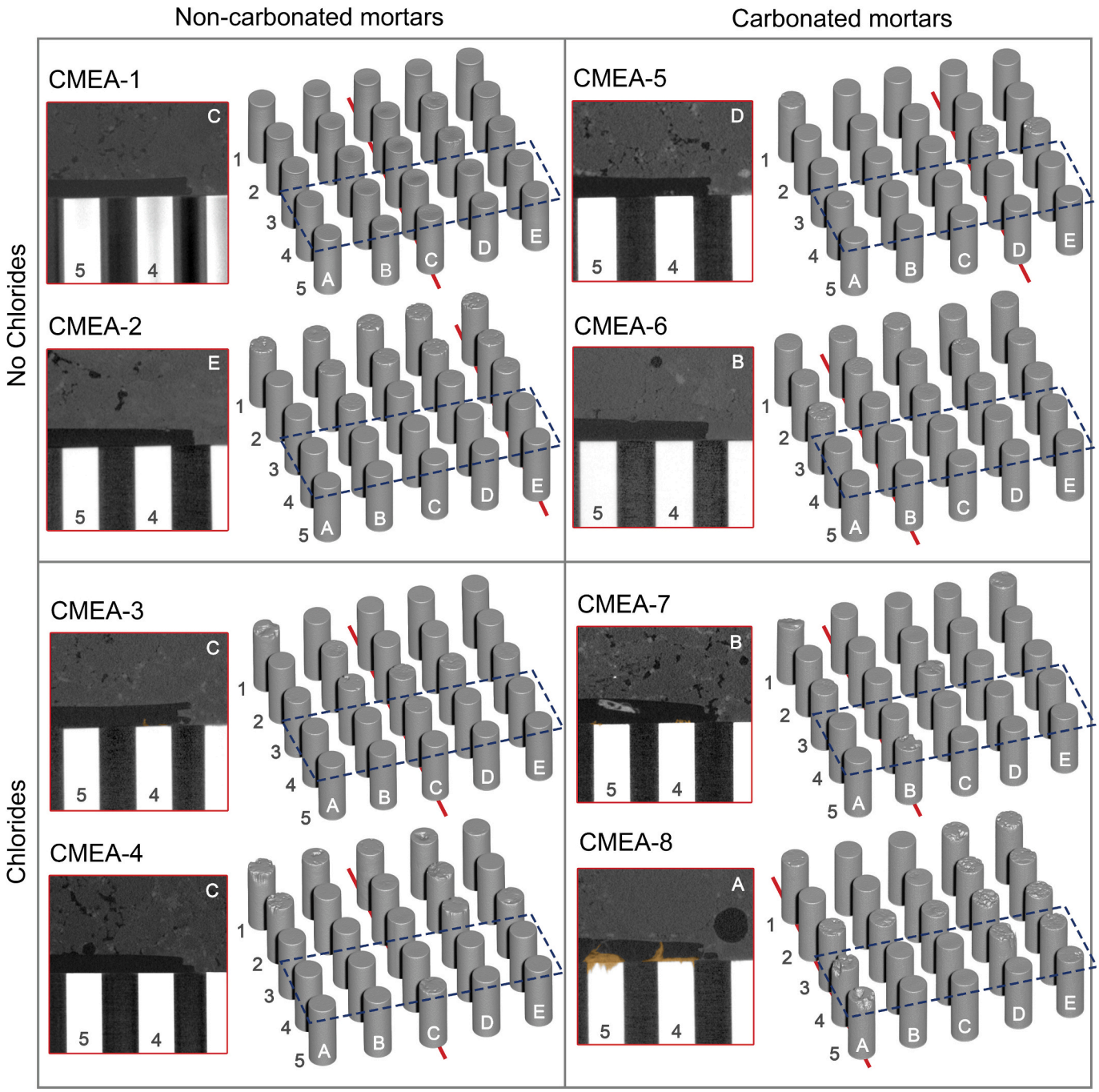

Fig. 9. A volumetric visual representation of the corrosion damage obtained using microCT (image on the right-hand side of each specimen) and a cross-sectional image of the electrodes with the mortar and void both visible (left-hand image in each quadrant). The electrodes positioned beneath the void are indicated in the rectangle marked with a blue dashed line, while the locations of the cross sections are indicated by the red lines underneath the 3D images.

mortar in either a non-carbonated or carbonated state. Half of the specimens were exposed to cyclic wetting with tap water, while the other half were exposed to cyclic wetting with a 3.5 % NaCl solution. This created four specific exposure environments (non-carbonated without chlorides, non-carbonated with chlorides, carbonated without chlorides and carbonated with chlorides), each consisting of 3 identical specimens in parallel.

The reduction in thickness of the ER sensors is shown in Fig. 10. The specimens are grouped in quadrants, with each quadrant representing a specific exposure environment and displaying all 3 identical specimens in parallel. The solid lines represent corrosion of the sensor under the mortar, while the dashed lines represent corrosion of the sensor under the artificially-produced void.

The lowest reduction in thickness was recorded on the non-carbonated specimens without chlorides (Fig. 10, upper left quadrant). Slightly higher corrosion rates (5 μm/year) were recorded on the ER-01 specimen under good contact with the mortar, while extremely low corrosion rates (1 μm/year) were recorded on all other specimens, both under the void and next to the mortar.

When chlorides were introduced to the non-carbonated mortars, the corrosion rates increased significantly (Fig. 10, bottom left quadrant). Corrosion first initiated on the sensors in good contact with the mortar, with corrosion rates of up to 220 μm/year recorded during the first 10 weeks of exposure. Sensors under the void corroded significantly slower

Table 2
Quantitative analysis of the CMEA and microCT damage volumes on select electrodes (10^6 μm^3).

Specimens	Carb.	Cl^-	Electrode	CMEA	microCT
CMEA-3		×	A1	2.7	3.2
CMEA-4		×	A1	1.6	2.3
CMEA-4		×	A2	3.8	3.2
CMEA-4		×	D2	1.5	2.4
CMEA-7	×	×	A1	8.2	11.1
CMEA-7	×	×	B5	1.8	2.1
CMEA-8	×	×	A5	5.7	6.2
CMEA-8	×	×	A4	3.9	5.8
CMEA-8	×	×	D3	3.6	4.0
CMEA-8	×	×	D4	3.6	4.6

during the same period, reaching average corrosion rates of only about 15 μm/year. After week 10, however, similar corrosion was observed on the sensors under the voids, reaching corrosion rates of 110 μm/year between weeks 15 and 20. Due to the nonlinear change in sensor thickness, it is expected that the corrosion was highly localised.

The carbonated specimens without chlorides (Fig. 10, upper right quadrant) first start to corrode where they were in good contact with the mortar. The corrosion rate was around 20 μm/year during the first 10 weeks of exposure, while no corrosion activity was recorded in the sensors under the void in the same timeframe. After about 15 weeks of exposure, the corrosion rates under the mortar increased significantly, up to 130 μm/year, while the sensors under the void also started to corrode, although at much slower corrosion rates of about 15 μm/year. Higher corrosion rates in the ER sensors under the void were only recorded after about 35 weeks of exposure, reaching rates between 20 and 50 μm/year, depending on the specimen.

The last combination of mortar properties studied were the carbonated mortars contaminated with chlorides (Fig. 10, bottom right quadrant). Corrosion first initiated where there was good contact with the mortar, with the corrosion rate reaching about 20 μm/year in all 3 specimens. After 10 weeks of exposure, corrosion initiated beneath the void in specimen ER-11, immediately reaching a high corrosion rate of 110 μm/year. The same phenomenon occurred beneath the void of specimen ER-10 after 25 weeks of exposure, where an even higher corrosion rate of 400 μm/year was detected. Throughout this period, and until the end of the exposure, moderate corrosion activity continued to occur on the sensors in good contact with the mortar, with corrosion rates varying between 20 and 60 μm/year.

3.2.2. Post-exposure microCT validation

Corrosion damage was scanned and assessed using microCT in order to validate the ER results, evaluate the shape and dimensions of the void, and to characterize the type of corrosion damage. The microCT results for 4 representative specimens are presented in Fig. 11, divided into groups based on the carbonation and chloride state of the mortar. For each specimen, a top-down view of the sensor at the end of exposure is shown on the left, and a cross section of the same sensor shown on the right. The electrodes positioned under the void are indicated by the rectangle marked with a blue dashed line. The microCT results for all other specimens are available in the supplementary material.

No corrosion damage was visible on any of the specimens made from non-carbonated mortars without chlorides. These results are expected, as corrosion rates of 5 um/year or lower will not cause significant corrosion damage over a 1-year period of exposure. Furthermore, any potential damage caused would be below the resolution threshold of the microCT scans. The specimens were also used to evaluate the width of the void, which, on average, was about 0.5 mm thick.

In the non-carbonated mortars contaminated with chlorides, severe damage was observed on all specimens, both under the mortar and beneath the void. This was as expected, based on the ER sensor analysis. In both cases the corrosion damage is localised, but near the void the damage is more clustered and concentrated around a single location, whereas under the mortar it occurs in the form of small pits. Observation of the cross sections reveals that the corrosion products fill the gap where the steel electrodes were initially located.

Significant corrosion only occurred on the electrodes in carbonated mortar without chlorides where there was good contact with the mortar. The corrosion seemed to be more uniformly distributed across the surface of the ER electrodes in these samples, covering about 50 % of the total sensor surface area. Only small traces of localised corrosion were visible on the electrodes positioned under the void. The damage was most pronounced on specimen ER-09. The cross-sectional images display the presence of some corrosion products, but in some locations the ER electrode has corroded, leaving the space it occupied now empty (ER-08).

In the carbonated mortar contaminated with chlorides, in 2 of the specimens (ER-10, ER-11) significantly more damage is observed on the ER electrodes under the void, while in specimen ER-12 there seems to be no corrosion at all beneath the void (available in the supplementary material). In the first 2 specimens the type of corrosion is very general, covering at least 70 % of the electrode's total surface area. The electrodes in contact with the mortar show comparatively less damage, and the damage is more localised, covering a smaller surface area than the damage beneath the voids. It is worth noting that the cross-sectional view of specimen ER-12 shows the formation of a very narrow void, which could explain the differing corrosion behaviour in this specimen.

4. Discussion

4.1. Spatial distribution of the corrosion

With regards to how the corrosion damage is distributed around any voids present on the steel concrete interface, researchers have found that damage can occur both inside and outside these features. Angst et al. [7] completed a comprehensive review of the steel-concrete interface in the presence of chlorides, and proposed that the water content inside the voids determines where corrosion is initiated. Specifically, only voids that are sufficiently saturated (which, for larger air voids in a real structure would typically take years to occur) will provide the necessary conditions for anodic locations to occur within a void. Other researchers [37,38] observed that corrosion often occurred inside and in proximity with interfacial air voids, implying that there are other factors at work. Glass et al. [39], for example, found that a decrease in the number of voids led to a proportionate decrease in the amount of corrosion damage, due to the buffering effect of hydroxyl ions in the cement paste, which covers a larger surface area of the steel in structures with less defects.

In the present research we found that, in most cases, corrosion damage first initiated outside the voids, where there was good contact with the mortar (the exceptions to this will be discussed later). This type of initiation aligns more with the saturation theory proposed by Angst et al. [7], as it would not be expected for the voids to be adequately saturated until a given number of wetting cycles had occurred. This happened after about 10–15 wetting cycles (Figs. 5, 7 and 10), at which point corrosion also started to initiate inside the voids, dependent on both the state of the mortar as well as the specimen type (the width of the voids being 0.3 mm and 0.5 mm, respectively). This would imply that, at this point, the voids were sufficiently saturated for corrosion processes to take place, suggesting that time plays an important role when assessing the occurrence of damage around voids and crevices. Furthermore, this theory does not contradict the research mentioned previously, where significant corrosion damage was found both within and in the vicinity of voids, as the specimens evaluated in that study were exposed for several years or even several decades.

The average corrosion rates followed the same trend as that observed with corrosion initiation, i.e. the average corrosion rates of electrodes under good contact with the mortar were initially higher than those of

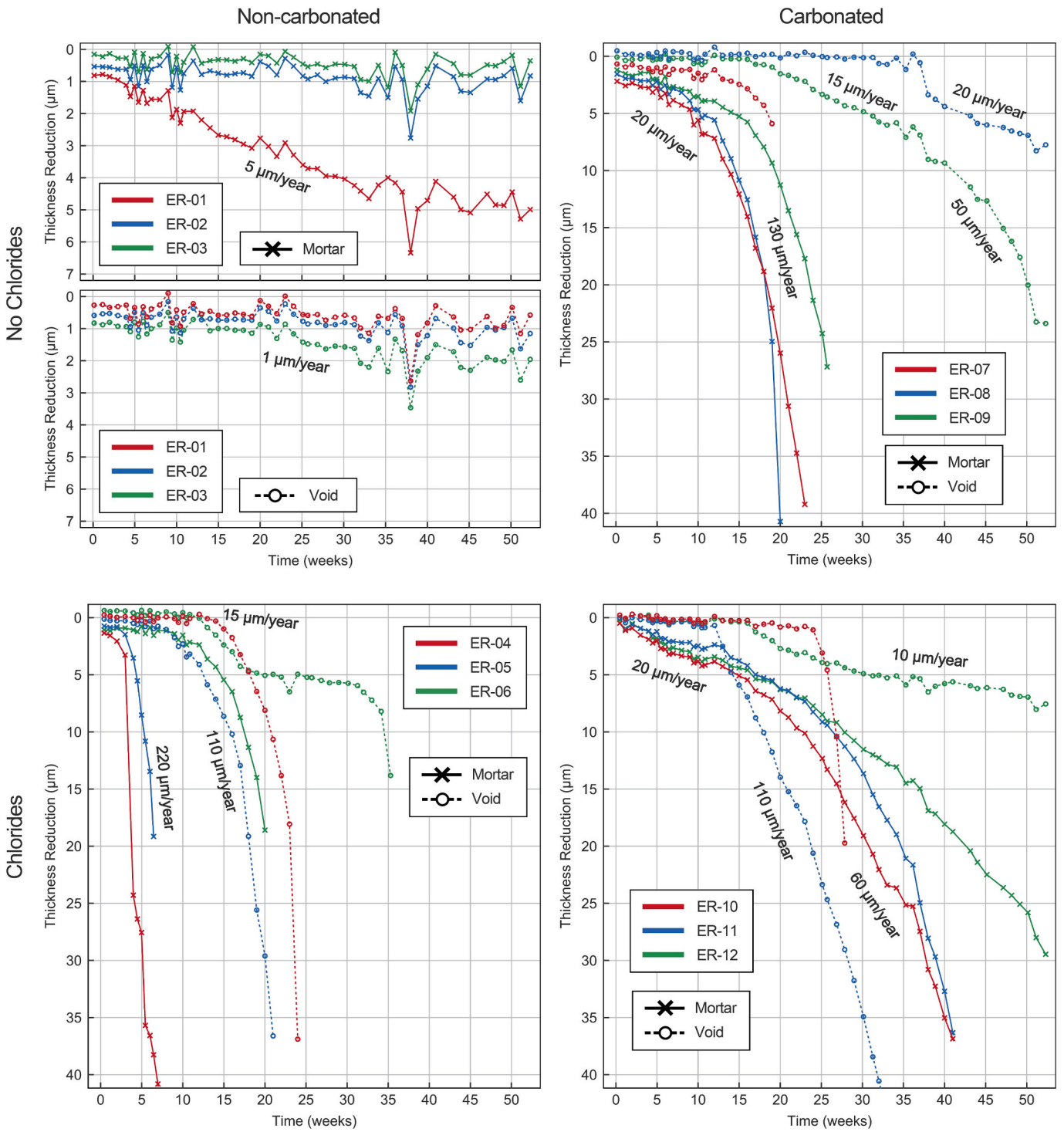

Fig. 10. ER sensor thickness reduction measurements for all ER specimens. Each quadrant represents a specific exposure environment and displays the 3 identical specimens in parallel.

the electrodes inside the voids. This is summarized in Fig. 12, where the average corrosion rates for each specimen are plotted, grouped according to the location (under the void or the mortar), the carbonation state and the presence of chlorides. On average, the rates of corrosion under the mortar were about a decade higher than those beneath the void. This difference was higher in the measurements determined by CMEA compared to the ER measurements, indicating that the width of the void played an important role in the corrosion rates measured. The CMEA technique generally detects localised corrosion with higher accuracy than the ER technique, so the differences in corrosion rate measurements could probably, in part, also be assigned to the characteristics of the measuring techniques. In the chloride mortars, corrosion rates on the electrodes positioned beside the voids became progressively higher as the period of exposure progressed beyond 25 weeks, achieving similar magnitudes to as those observed directly beneath the mortar (Fig. 10). The research mentioned previously [37], conducted on 20 year old specimens, found that the corrosion damage next to the voids was the most severe, which would imply that the corrosion rates inside the

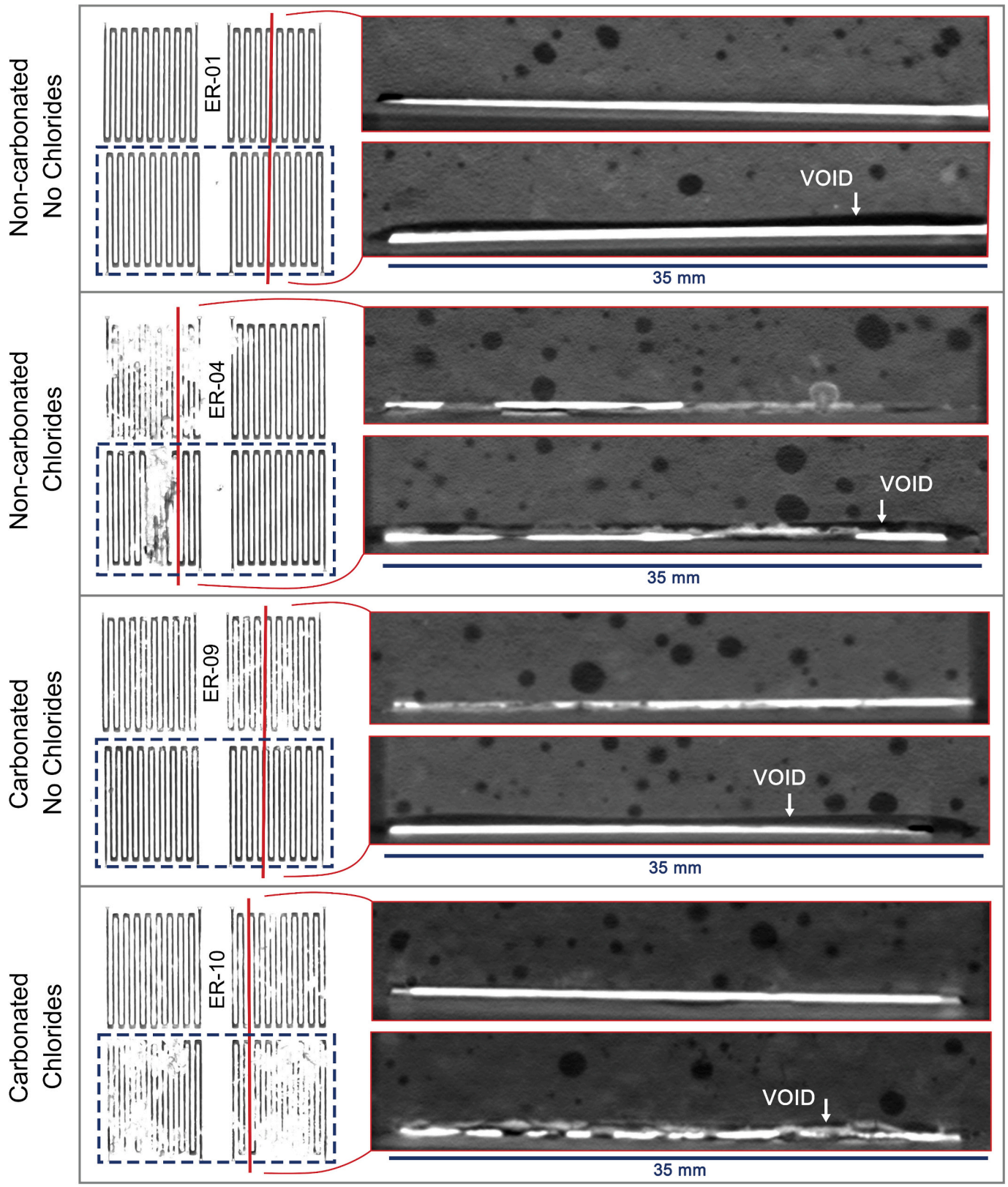

Fig. 11. Visual representation of the corrosion damage on 4 representative ER specimens obtained using the microCT technique, and characteristic cross sections (in red bordered rectangles) showing the artificially produced void, the mortar and the ER sensor. Location of the cross-section is shown by a red solid line on the left. The ER elements positioned under the void are indicated by the rectangle marked with a blue dashed line. (For interpretation of the references to colour in this figure legend, the reader is referred to the web version of this article.)

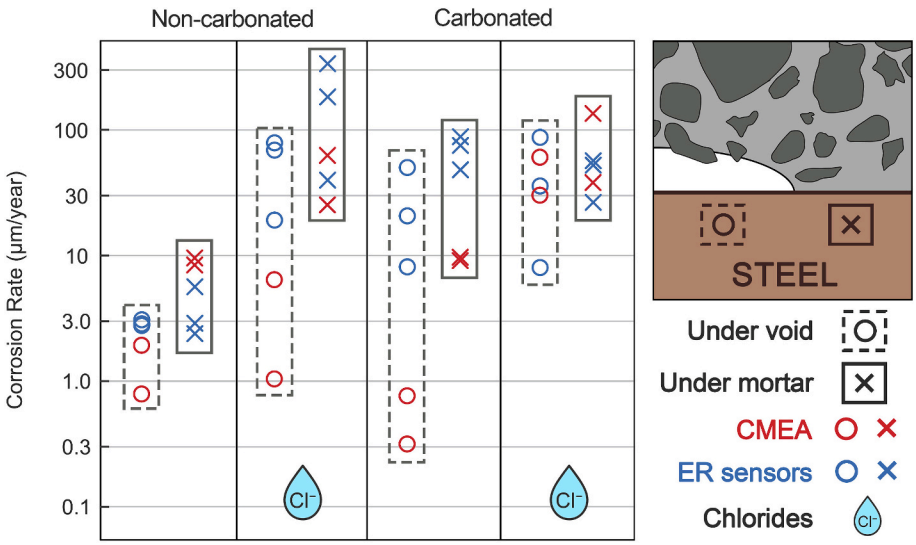

Fig. 12. An overview of the average corrosion rates obtained from the CMEA and ER techniques, grouped according to the carbonation state, the presence of chlorides (as indicated by the blue chloride droplet icon), the technique used (red versus blue) and the type of contact (next to the void shown by the dashed lines and circles, whereas contact with the mortar is indicated by the solid lines and crosses). (For interpretation of the references to colour in this figure legend, the reader is referred to the web version of this article.)

voids could continue to increase over many years, as the voids become progressively more saturated with chlorides. It is important to note that there was significant scatter with respect to the corrosion rates inside the voids, which would likely indicate that influential factors not monitored during this research were in play.

One often overlooked aspect not shown by Fig. 12 is the location of the cathodic reactions, which can be seen using the CMEA technique. Surprisingly, in most specimens, the steel area directly beneath the void did not participate significantly in the current exchange, with only very minor cathodic or anodic currents detected in this area. One of the more common corrosion-related theories connected to air-filled voids on the steel-concrete interface is the suggestion that air trapped inside the void provides a sufficient supply of oxygen for the cathodic reaction. These results show that, at least during the early onset of corrosion and corrosion initiation, the oxygen inside the air void is not usually reduced. Rather, it either stays dormant and seldomly participates in the redox reaction, slowly permeates inside the concrete pore structure towards the cathodic sites, or becomes dissolved in the solution as the void becomes slowly saturated. It appears that the void and mortar can act as separate electrochemical systems until either sufficient saturation time passes, or certain conditions regarding the pH and chloride levels on the steel surface are met (see Section 4.3 Effects of chlorides and carbonation). Once these conditions occur, electrodes both under the mortar and beneath the void can pass from the anodic to the cathodic side (and vice versa) during a single wetting and drying period, as is the case in Fig. 8d.

4.2. Void geometry and location

Another topic regarding the influence of voids on the steel-concrete interface which is seldomly discussed is the void geometry. More specifically, what is the width of the void where corrosion stops behaving like corrosion in a bulk pore solution and starts behaving more like crevice corrosion? A group of papers [40–42] conducted in a simulated concrete environment examined corrosion processes inside a tapered crevice of variable thickness. It was discovered that at both the mouth of the crevice (3 mm) and near the tip of the crevice (0.3 mm), the corrosion current was in fact cathodic, while currents in the middle of the tapered crevice were anodic. This behaviour is more common for a bulk solution, as crevice corrosion usually promotes anodic activities close to the tip, where oxygen depletion is highest and diffusion of the bulk solution is lowest [43]. Recently, a study on crevice corrosion in steel liners in concrete was also published [17]. Generally, the crevice corrosion evident was found where there was close contact between the mortar and the steel, while a gap of 1 mm had no effect on the type of corrosion.

The width of the gap used in this research was verified using microtomography, and was shown to be around 0.3 mm for the CMEA specimens and 0.5 mm for the ER specimens (Figs. 9 and 11). Based on the research mentioned above and the results obtained in this study, we believe that this width is not sufficient to promote crevice corrosion. Gaps much smaller than 0.1 mm are likely needed for crevice corrosion experiments. It is, however, not clear how the transport of water, oxygen and chlorides through crevice walls contributes to the typical crevice corrosion mechanism along a crevice. In addition, the following question arises: if the width of the gap needs to be particularly small to promote crevice corrosion, what if a crevice was unintentionally formed where there was good contact with the mortar? This would partly explain the more anodic behaviour of the steel under the mortar, but the lack of cathodic reactions directly beneath the void (i.e. in the bulk solution) remains unexplained. Either way, a gap of 10 µm or smaller would not be accurately detected using the current specimen sizes and microCT technology, so smaller CMEA specimens, both in terms of the size of the electrodes and the overall dimensions, would be needed to test the effects of such crevice corrosion.

4.3. Effects of chlorides and carbonation

As part of the experimental phase, both carbonation and chlorides were used to initiate corrosion. This resulted in 4 unique mortar states: non-carbonated without chlorides, non-carbonated with chlorides, carbonated without chlorides and carbonated with chlorides. If we look back at Fig. 10 and Fig. 12, we can observe that most of the corrosion behaviour discussed so far generally applies to all four of the mortar states. The average corrosion rates during the first 26 weeks of exposure were higher where there was good contact with the mortar compared to in the electrodes in contact with the void, while the corrosion rates by the void comparatively increased during the second half of the exposure period. In most cases corrosion also initiated beneath the mortar first. Chloride-contaminated mortars exhibited more localised corrosion, with higher average corrosion rates and slower drying capabilities, due to the higher water retention, all of which are known effects of chloride

contamination [44,45]. There are, however, some specific aspects to each mortar state, such as initiation times and participation of the void steel surface, which will be discussed next.

Initiation times were generally much faster in the chloride-contaminated concrete, suggesting that the build-up of sufficient chloride for depassivation occurred much faster than the build-up of sufficient moisture required in the mortars not contaminated with chlorides. This was true when using both the CMEA and ER techniques, where corrosion initiated within the first week of exposure in the chloride-contaminated mortars, while it took roughly 8 to 10 weeks of exposure for the non-chloride specimens to indicate any significant corrosion activity. This was true even in the case where there were no chloride ions or carbonation present. Corrosion in this environment likely occurred due to a relatively high water-to-cement ratio resulting in a higher-than-normal total porosity, which allowed water and oxygen to permeate quickly towards the steel surface, and the presence of features on the steel-concrete interface (pores, voids, mill scale, cracks, etc.).

Generally, the steel surface under the void did not show any significant participation in current exchange until later in the exposure period (around the 15th week). The only exception to this was the carbonated and chloride-contaminated mortar, where corrosion initiated and achieved high corrosion rates under the void first. One explanation for this behaviour could be the previously-mentioned buffering effect of the hydroxyl ions [39] where there was good contact with the mortar, where slightly higher pH values are present locally in direct contact with the cement paste. The void, on the other hand, contained both the lower pH solution and chlorides representative of the bulk pore solution, which depassivated the steel faster and produced anodic locations. Additionally, we have previously shown in pore solution experiments that the combination of carbonated mortar and chlorides tends to depassivate steel more evenly and produce more unstable corrosion products, further increasing corrosion [46,47]. It was resolved that, in these specimens, the combined exposure to carbonation and chlorides initiated fairly intensive corrosion processes that generated a distinct layer of corrosion products. Presumably, this layer reduced the width of the void, and would consequently induce a kind of crevice corrosion process over time.

4.4. Proposed corrosion mechanisms

Based on the results discussed, specific environmental corrosion mechanisms are proposed that potentially take place around voids during initiation, during early corrosion propagation, before the voids have become sufficiently saturated with electrolytes, and during late corrosion propagation. Models proposed for the locations of the cathodic and anodic sites around the voids are presented in Fig. 13. The red crosses represent the anodic sites, while the green crosses represent the cathodic sites.

With mechanism (a), the anodic and cathodic sites are both located under the mortar. This mechanism was predominantly found in the mortars not contaminated with chlorides and occurred before the voids became sufficiently saturated with the solution. This mechanism was typically only in effect during the wetting periods, with its effect completely diminished during the drying period. The current densities that represent this mechanism were adapted from Fig. 5d.

Mechanism (b) was generally observed in the chloride-contaminated concretes with non-saturated voids. The anodic and cathodic sites were predominantly found under the mortar, but non-negligible cathodic currents could also appear inside the void. This mechanism was present during both the wetting and drying phases, as the chloride-contaminated mortar could not sufficiently dry out between wetting cycles. The current densities that represent this mechanism were adapted from Fig. 6d.

With mechanism (c) the anodic and cathodic currents are distributed roughly equally between inside the void and under the mortar. This was only observed in the carbonated mortars contaminated with chlorides, and the mechanism was present during both the wetting and drying periods. As mentioned previously, with this mechanism certain electrodes passed from one state to another (i.e. anodic to cathodic or vice versa), either during the wetting and drying periods or within a single wetting period. This implies that an electrochemical cell developed between the void and under the mortar, but under specific conditions during wetting and drying, two separate electrochemical cells might also exist. It is also believed that a process similar to mechanism (c) could also be present in mortars with sufficiently saturated voids. This would explain the severe corrosion damage found under voids and concrete defects in structures over longer periods of exposure [6,7]. This could not be proven in this study, however, as the CMEA experiments were not long enough for such mortar states to be obtained. The current densities that represent this mechanism were adapted from Fig. 8d.

5. Conclusions

Corrosion phenomena that occur around voids at the steel-concrete interface (SCI) were thoroughly studied and evaluated. The evolution of corrosion processes was monitored using the coupled multi-electrode array (CMEA) technique and electrical resistance (ER) sensors, and the corrosion damage following exposure was assessed by microCT. Corrosion was initiated by wetting with chloride ions and using carbonation, creating 4 specific exposure environments: non-carbonated without chlorides, non-carbonated with chlorides, carbonated without chlorides and carbonated with chlorides. The following conclusions summarize the most important findings:

1. The width of the void (between 0.3 and 0.5 mm) was assessed to promote corrosion similar to that found in air voids and larger cracks. In most mortar specimens, corrosion damage first initiated outside of the voids, where there was good contact with the mortar. The average corrosion rates were also generally higher under the mortar as opposed to inside the voids. Inadequately saturated voids were found to be the most likely cause of this corrosion behaviour.
2. Although certain indications of crevice corrosion were expected with formation of the void, this type of corrosion was not observed. It might be assumed that the width of the void was too large, since no clear separation was detected between the anodic and cathodic sites beneath the void and under the mortar.
3. Chloride contamination had some predictable and known effects on corrosion: more localised corrosion occurred with faster corrosion initiation and higher average corrosion rates, while the drying capability of the mortar was lower. When the carbonated mortar was contaminated with chlorides, corrosion initiated and achieved high corrosion rates under the void first. This was in contrast to the other mortar conditions, where both the anodic and cathodic activity was more pronounced under the mortar.
4. Throughout the phases of corrosion initiation and early propagation, the steel beneath the voids barely participated in the electrochemical reactions. The only exception to this was the carbonated mortar contaminated with chlorides. It seems that the void and mortar can act as separate electrochemical cells until either enough saturation time passes or certain conditions regarding the pH and chloride levels on the steel surface are fulfilled.
5. Three different corrosion mechanisms were proposed, taking into account the locations of the anodic and cathodic sites relative to the position of voids. The individual mortars with differing carbonation states and levels of chloride contamination were evaluated with respect to the most feasible mechanisms for corrosion initiation and early propagation.
6. Since a fairly long wetting period may be required to saturate the voids, our outcomes could not be directly extrapolated to the long-term evolution of corrosion. In addition, the growth of corrosion products can also affect these processes, either in terms of the corrosion rate or the localization of anodic and cathodic sites. These

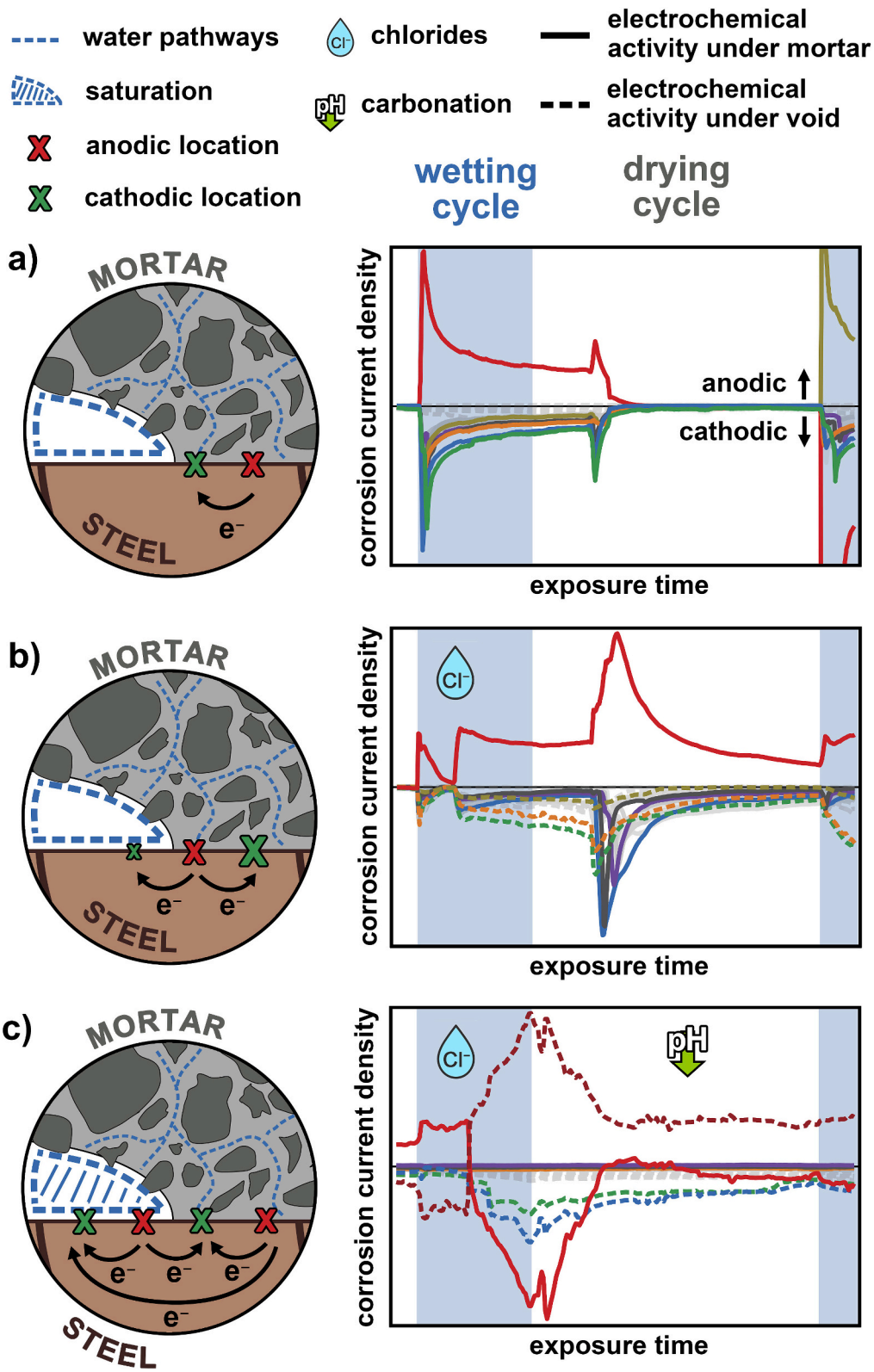

Fig. 13. The proposed models for the location of cathodic and anodic sites around voids at the steel-concrete interface. The red crosses indicate the anodic sites, green crosses indicate the cathodic sites, and the dashed blue lines indicate adsorbed water on the surface of the void and in the cement matrix: (a) anodic and cathodic sites are both located under the mortar, (b) anodic sites are located under the mortar and cathodic sites are located both under the mortar and beneath the void, but with a higher amount under the mortar, (c) anodic and cathodic sites are located both under the void and beneath the mortar in roughly equal amounts. Anodic and cathodic y-axis are not in scale to better visualise corrosion activity. (For interpretation of the references to colour in this figure legend, the reader is referred to the web version of this article.)

issues should take considerable attention in further research, through the implementation of longer exposure periods and additional analytical techniques.

CRediT authorship contribution statement

Miha Hren: Writing – original draft, Visualization, Validation, Resources, Project administration, Methodology, Investigation, Funding acquisition, Data curation, Conceptualization. **Tadeja Kosec:** Writing – review & editing, Validation, Supervision, Project administration, Conceptualization. **Andraž Legat:** Writing – review & editing, Supervision, Project administration, Methodology, Funding acquisition, Conceptualization.

Declaration of competing interest

The authors declare the following financial interests/personal relationships which may be considered as potential competing interests: Miha Hren reports financial support was provided by the Slovenian Research and Innovation Agency (ARIS). If there are other authors, they declare that they have no known competing financial interests or personal relationships that could have appeared to influence the work reported in this paper.

Data availability

Data will be made available on request.

Acknowledgements

The authors acknowledge financial support from the Slovenian Research and Innovation Agency (postdoc project No. Z2-2641 and research core funding No. P2-0273) and the ACES H2020 Euratom project (Grant agreement ID: 900012).

Declaration of Generative AI and AI-assisted technologies in the writing process

During the preparation of this work the author(s) used ChatGPT in order to improve the written language. After using this tool/service, the author(s) reviewed and edited the content as needed and take(s) full responsibility for the content of the publication.

Appendix A. Supplementary data

Supplementary data to this article can be found online at https://doi.org/10.1016/j.cemconres.2024.107545.

References

[1] R. Cigna, U. Nürnberger, C. Andrade, R. Polder (Eds.), Corrosion of steel in reinforced concrete structures: COST action 521; final report, Office for Official Publications of the European Communities, Luxembourg, 2003.
[2] L. Bertolini, B. Elsener, P. Pedeferri, E. Redaelli, R.B. Polder, Corrosion of Steel in Concrete: Prevention, Diagnosis, Repair, Wiley-VCH Verlag GmbH & Co., Weinheim, Germany, 2013. https://doi.org/10.1002/9783527651696 (accessed July 8, 2016).
[3] U. Angst, B. Elsener, C.K. Larsen, Ø. Vennesland, Critical chloride content in reinforced concrete - a review, Cem. Concr. Res. 39 (2009) 1122–1138, https://doi.org/10.1016/j.cemconres.2009.08.006.
[4] M. Pourbaix, Atlas of Electrochemical Equilibria in Aqueous Solutions, 2nd edition, National Association of Corrosion Engineers, Houston, Texas, 1974.
[5] C.L. Page, Mechanism of corrosion protection in reinforced concrete marine structures, Nature 258 (1975) 514–515, https://doi.org/10.1038/258514a0.
[6] U.M. Angst, M.R. Geiker, A. Michel, C. Gehlen, H. Wong, O.B. Isgor, B. Elsener, C. M. Hansson, R. François, K. Hornbostel, R. Polder, M.C. Alonso, M. Sanchez, M. J. Correia, M. Criado, A. Sagüés, N. Buenfeld, The steel–concrete interface, Mater. Struct. 50 (2017), https://doi.org/10.1617/s11527-017-1010-1.
[7] U.M. Angst, M.R. Geiker, M.C. Alonso, R. Polder, O.B. Isgor, B. Elsener, H. Wong, A. Michel, K. Hornbostel, C. Gehlen, R. François, M. Sanchez, M. Criado, H. Sørensen, C. Hansson, R. Pillai, S. Mundra, J. Gulikers, M. Raupach, J. Pacheco, A. Sagüés, The effect of the steel–concrete interface on chloride-induced corrosion initiation in concrete: a critical review by RILEM TC 262-SCI, Mater. Struct. 52 (2019) 88, https://doi.org/10.1617/s11527-019-1387-0.
[8] E. McCafferty, Introduction to Corrosion Science, Springer, New York, 2010, https://doi.org/10.1007/978-1-4419-0455-3 (accessed July 8, 2016).
[9] G.S. Frankel, N. Sridhar, Understanding localized corrosion, Mater. Today 11 (2008) 38–44, https://doi.org/10.1016/S1369-7021(08)70206-2.
[10] R.D. Moser, P.M. Singh, L.F. Kahn, K.E. Kurtis, D.G. Niño, Z.B. McClelland, Crevice corrosion and environmentally assisted cracking of high-strength duplex stainless steels in simulated concrete pore solutions, Construct. Build Mater. 203 (2019) 366–376, https://doi.org/10.1016/j.conbuildmat.2019.01.082.
[11] J.A. Gonzalez, A. Molina, E. Otero, W. López, On the mechanism of steel corrosion in concrete: the role of oxygen diffusion, Mag. Concr. Res. 42 (1990) 23–27, https://doi.org/10.1680/macr.1990.42.150.23.
[12] G.N. Flint, R.N. Cox, The resistance of stainless steel partly embedded in concrete to corrosion by seawater, Mag. Concr. Res. 40 (1988) 13–27, https://doi.org/10.1680/macr.1988.40.142.13.
[13] R.M. Ghantous, R. François, S. Poyet, V. L'hostis, F. Bernachy-Barbe, D. Meinel, L. Portier, N.-C. Tran, Relation between crack opening and extent of the damage induced at the steel/mortar interface, Construct. Build Mater. 193 (2018) 97–104, https://doi.org/10.1016/j.conbuildmat.2018.10.176.
[14] L. Yan, G.-L. Song, Z. Wang, D. Zheng, Crevice corrosion of steel rebar in chloride-contaminated concrete, Construct. Build Mater. 296 (2021), https://doi.org/10.1016/j.conbuildmat.2021.123587.
[15] A. Sagüés, J. Fernandez, 2668: modeling nuclear containment liner steel liner, Corrosion 11 (2013).
[16] D. Dunn, A. Pulvirenti, P. Klein, Containment liner corrosion, in: J.T. Busby, G. Ilevbare, P.L. Andresen (Eds.), Proc. 15th Int. Conf. Environ. Degrad. Mater. Nucl. Power Syst. — Water React, Springer International Publishing, Cham, 2016, pp. 1037–1049, https://doi.org/10.1007/978-3-319-48760-1_63.
[17] E. Huttunen-Saarivirta, E. Bohner, A. Trentin, M. Ferreira, A closer look at the corrosion of steel liner embedded in concrete, Cem. Concr. Compos. 144 (2023) 105280, https://doi.org/10.1016/j.cemconcomp.2023.105280.
[18] Council Directive 2011/70/Euratom of 19 July 2011 establishing a Community framework for the responsible and safe management of spent fuel and radioactive waste. http://data.europa.eu/eli/dir/2011/70/oj/eng, 2011 (accessed January 24, 2020).
[19] Council Directive 2009/71/Euratom of 25 June 2009 establishing a Community framework for the nuclear safety of nuclear installations. http://data.europa.eu/eli/dir/2009/71/oj/eng, 2009 (accessed January 24, 2020).
[20] A. Česen, T. Kosec, A. Legat, Characterization of steel corrosion in mortar by various electrochemical and physical techniques, Corros. Sci. 75 (2013) 47–57, https://doi.org/10.1016/j.corsci.2013.05.015.
[21] M. Hren, T. Kosec, A. Legat, Characterization of steel corrosion processes in various blended cements by means of coupled multi-electrode arrays, Cem. Concr. Res. 168 (2023) 107134, https://doi.org/10.1016/j.cemconres.2023.107134.
[22] M. Hren, T. Kosec, A. Legat, Characterization of stainless steel corrosion processes in mortar using various monitoring techniques, Construct. Build Mater. 221 (2019) 604–613, https://doi.org/10.1016/j.conbuildmat.2019.06.120.
[23] T. Kosec, M. Hren, A. Legat, Monitoring copper corrosion in bentonite by means of a coupled multi-electrode array, Corros. Eng. Sci. Technol. 52 (2017) 70–77, https://doi.org/10.1080/1478422X.2017.1312200.
[24] F. Bocher, F. Presuel-Moreno, N.D. Budiansky, J.R. Scully, Coupled multielectrode investigation of crevice corrosion of AISI 316 stainless steel, Electrochem. Solid St. 10 (2007) C16–C20, https://doi.org/10.1149/1.2409747.
[25] F. Bocher, F. Presuel-Moreno, J.R. Scully, Investigation of crevice corrosion of AISI 316 stainless steel compared to Ni–Cr–Mo alloys using coupled multielectrode arrays, J. Electrochem. Soc. 155 (2008) C256–C268, https://doi.org/10.1149/1.2883741.
[26] N.D. Budiansky, F. Bocher, H. Cong, M.F. Hurley, J.R. Scully, Use of coupled multi-electrode arrays to advance the understanding of selected corrosion phenomena, Corrosion 63 (2007) 537–554, https://doi.org/10.5006/1.3278405.
[27] A. Legat, Monitoring of steel corrosion in concrete by electrode arrays and electrical resistance probes, Electrochim. Acta 52 (2007) 7590–7598, https://doi.org/10.1016/j.electacta.2007.06.060.
[28] S. Brisard, M. Serdar, P.J.M. Monteiro, Multiscale X-ray tomography of cementitious materials: a review, Cem. Concr. Res. 128 (2020) 105824, https://doi.org/10.1016/j.cemconres.2019.105824.
[29] EN 197-1:2011, Cement. Composition, specifications and conformity criteria for common cements, 2011.
[30] EN 196-1:2016, Methods of testing cement. Determination of strength, 2016.
[31] A. Česen, T. Kosec, A. Legat, V. Bokan-Bosiljkov, Corrosion properties of different forms of carbon steel in simulated concrete pore water, Mater. Technol. 48 (2014) 51–57.
[32] L. Yang, N. Sridhar, C.S. Brossia, D.S. Dunn, Evaluation of the coupled multielectrode array sensor as a real-time corrosion monitor, Corros. Sci. 47 (2005) 1794–1809, https://doi.org/10.1016/j.corsci.2004.08.002.
[33] A. Naganuma, K. Fushimi, K. Azumi, H. Habazaki, H. Konno, Application of the multichannel electrode method to monitoring of corrosion of steel in an artificial crevice, Corros. Sci. 52 (2010) 1179–1186, https://doi.org/10.1016/j.corsci.2010.01.005.
[34] ASTM, ASTM G102–89: Standard Practice for Calculation of Corrosion Rates and Related Information from Electrochemical Measurements, 2016.
[35] T. Kosec, V. Kuhar, A. Kranjc, V. Malnarič, B. Belingar, A. Legat, Development of an electrical resistance sensor from high strength steel for automotive applications, Sensors 19 (2019) 1956, https://doi.org/10.3390/s19081956.

[36] A. Legat, M. Leban, Ž. Bajt, Corrosion processes of steel in concrete characterized by means of electrochemical noise, Electrochim. Acta 49 (2004) 2741–2751, https://doi.org/10.1016/j.electacta.2004.01.036.
[37] E. Rossi, R. Polder, O. Copuroglu, T. Nijland, B. Šavija, The influence of defects at the steel/concrete interface for chloride-induced pitting corrosion of naturally-deteriorated 20-years-old specimens studied through X-ray computed tomography, Construct. Build Mater. 235 (2020) 117474, https://doi.org/10.1016/j.conbuildmat.2019.117474.
[38] W.H. Hartt, J.-H. Nam, L. Li, Critical Issues Related to Corrosion Induced Deterioration Projection for Concrete Marine Bridge Substructures. https://trid.trb.org/view/731119, 2002 (accessed November 5, 2023).
[39] G.K. Glass, B. Reddy, L.A. Clark, Making reinforced concrete immune from chloride corrosion, Proc. Inst. Civ. Eng. - Constr. Mater. 160 (2007) 155–164, https://doi.org/10.1680/coma.2007.160.4.155.
[40] Y. Guo, Investigation of crevice corrosion behavior of HRB355 steel in 3.5% NaCl solution using coupled multi-electrode arrays, Int. J. Electrochem. Sci. 16 (2021) 1–11, https://doi.org/10.20964/2021.08.47.
[41] G. Li, D. Yin, J. Pang, Investigation of failure behavior of HRB335 steel due to crevice corrosion in concrete using electrochemical method, Int. J. Electrochem. Sci. 16 (2021) 1–11, https://doi.org/10.20964/2021.11.53.
[42] J. Chen, L. Ji, J. Song, Study of crevice corrosion behavior and cathodic protection of carbon steel reinforcement in concrete, Int. J. Electrochem. Sci. 17 (2022), https://doi.org/10.20964/2022.01.01.
[43] A. Turnbull, Theoretical evaluation of the dissolved oxygen concentration in a crevice or crack in a metal in aqueous solution, Br. Corros. J. 15 (1980) 162–171, https://doi.org/10.1179/000705980798275229.
[44] M. Hren, V. Bokan Bosiljkov, A. Legat, Effects of blended cements and carbonation on chloride-induced corrosion propagation, Cem. Concr. Res. 145 (2021) 106458, https://doi.org/10.1016/j.cemconres.2021.106458.
[45] Y. Wang, H. Oleiwi, C.-Y. Wang, N. Xiang, J. Geng, The characterization of chloride effect on concrete water sorption and its application in the modelling of concrete conditions in tidal zones, Construct. Build Mater. 253 (2020) 119074, https://doi.org/10.1016/j.conbuildmat.2020.119074.
[46] M. Hren, T. Kosec, A. Legat, V. Bokan-Bosiljkov, Corrosion performance of steel in blended cement pore solutions, Mater. Technol. 53 (2019) 679–686, https://doi.org/10.17222/mit.2019.003.
[47] M. Hren, T. Kosec, A. Legat, Corrosion behavior of steel in pore solutions extracted from different blended cements, Mater. Corros. 71 (2020) 759–766, https://doi.org/10.1002/maco.202011548.